Electron energy-loss spectroscopy of $LiMn_2O_4$, $LiMn_{1.6}Ti_{0.4}O_4$ and $LiMn_{1.5}Ni_{0.5}O_4$

F. Espinosa-Magaña, L. Alvarez-Contreras, O. Morales-Rivera, M.T. Ochoa-Lara, S.M. Loya-Mancilla, A. Aguilar-Elguezabal.

Abstract

The dielectric properties of $LiMn_2O_4$, $LiMn_{1.6}Ti_{0.4}O_4$ and $LiMn_{1.5}Ni_{0.5}O_4$ powders, synthesized by sol–gel method, were determined by analyzing the low-loss region of the electron energy-loss spectroscopy (EELS) spectrum in a transmission electron microscope. From these data, the optical joint density of states (OJDS) was obtained by Kramers–Kronig analysis. Since maxima observed in the OJDS spectra are assigned to interband transitions above the Fermi level, these spectra can be interpreted on the basis of calculated density of states (DOS), carried out with the CASTEP code. Experimental and theoretical results are in good agreement.

Keywords: Oxides, sol-gel growth, *Ab initio* calculations, Electron energy-loss spectroscopy (EELS), Dielectric properties.

Introduction

The use of rechargeable batteries has become a standard for mobile applications, being, for many years, $LiCoO_2$ the most common material used for the cathode. However, the toxicity of cobalt and its high cost has stimulated the search for alternative materials to substitute cobalt by a cheaper and environmentfriendly material. One of the most promising materials to fulfill these requirements is the $LiMn_2O_4$ spinel [1–3]. Recently, several new spinel manganates, where the Mn 16d site of the spinel

structure is partially substituted by a third cation, have been studied extensively and the electrochemical properties and crystal structure of these substituted materials have been reported [4–10]. These materials overcome the disadvantages of stoichiometric $LiMn_2O_4$ spinel, while still possessing a spinel structure.

Whereas numerous experimental investigations were devoted to electrochemical characteristic of the lithium-based cell, more recent studies (see [11] and references therein) were aimed to investigate structural, electronic, magnetic and optical properties of the spinel-type lithium manganese oxides. Suzuki et al. [12] applied electron energy-loss spectroscopy (EELS) to analyze the valence of transition metal ions in spinel $LiMn_2O_4$ (M = Ti, Cr, Mn, Co), Shiraishi et al. [13] studied the substituted spinels $LiMn_{1.6}M_{0.4}O_4$ (M = Co, Cr, Ni). These works were focused on the analysis of transition metals ionization edges in the high-energy-loss region of EELS spectra. More recently, Kim and Lee [14] studied the effect of nickel doping on structural and optical properties of lithium manganate thin films by optical methods. However, studies in the low-energy-loss region of substituted spinels seem to be absent in the literature, even though it is recognized that basic understanding of electronic structure and chemical bonding of electrode materials, which underlies the electrochemical behavior of the battery, is indispensable for the development of advanced electrode materials.

Electron energy-loss spectroscopy has been widely used to study the composition and electronic structure of materials [15–17]. The interactions of fast electrons with the specimen result in excitations of electrons into unoccupied energy levels in the conduction band as well as collective excitations of valence electrons.

Interband transitions originate from the excitation of electrons in the valence band to empty states in the conduction bands, so these can be identified as transitions in a band structure model. EELS can be used to probe the electronic structure of materials, and it has been widely applied as fingerprint studies, allowing the identification of phases by comparison with wellknown spectra. In the high-energy-loss region, analysis of the first 10 eV of the spectra after the ionization edge (ELNES) can give information about the oxidation state, the absolute energy position and local symmetry via d level splittings in transition metal elements and orbital hybridization. The low-loss region can provide information about composition and electronic structure, as well as optical properties, although it has not found as wide applications as ELNES. This relies on the well-known fact that lowlosses originate from all possible transitions between the valence band and the conduction band. The valence band is made up of dispersed levels, as opposed to almost flat core levels, and interpretation of EELS spectra is a priori more difficult.

To our knowledge, low-energy-loss EELS has not been used for studies of $LiMn_{1.6}Ti_{0.4}O_4$ and $LiMn_{1.5}Ni_{0.5}O_4$ yet. In this work, we have conducted low-energy-loss EELS on sol–gel synthesized $LiMn_2O_4$, $LiMn_{1.6}Ti_{0.4}O_4$ and $LiMn_{1.5}Ni_{0.5}O_4$ powders, obtaining the complex dielectric function and the optical joint density of states (OJDS) by Kramers–Kronig analysis. A comparison is made with theoretical results based on energy-band structure calculations.

From the dielectric theory, it is possible to relate the experimental single scattering distribution S(E) to the energy-loss function Im(-1/ε), by [15]

$$S(E) = \frac{I_0 t}{\pi a_0 m_0 v^2} \mathrm{Im}\left[-\frac{1}{\varepsilon(q,E)}\right] \ln[1+(\beta/\theta_E)^2] \qquad (1)$$

where $\varepsilon(q,E) = \varepsilon_1+i\varepsilon_2$ is the complex dielectric function at energy loss E and momentum transfer q, a_0 the Bohr radius, m_0 the electron rest mass, *v* the electron beam velocity, θ the scattering angle and $\theta_E = E/(\gamma m_o v^2)$ is the characteristic scattering angle, γ is the relativistic factor, I_0 is the zero loss intensity, t the specimen thickness and β is the collection semi-angle.

As peak positions in the energy-loss spectrum at low-energy losses are strongly influenced by the volume plasmon and the positions of other excitations, the energy-loss spectrum, obtained from Eq. (1), cannot be directly associated with interband transitions. However, the imaginary part of the dielectric function $\varepsilon_2(E)$ can be associated with interband transitions. The real and imaginary parts of the dielectric function can be obtained from the energy-loss function through Kramers–Kronig analysis.

To compare the experimental results from EELS with the density of states (DOS) obtained from band theory calculations, we can define the optical joint density of states, as [18–20]

$$J_1(E) = \frac{2E\varepsilon_2(E)}{\pi E_p^2} \qquad (2)$$

where E_p is the plasmon energy in Drude model

$$E_p^2 = \frac{\hbar^2 n e^2}{\varepsilon_0 m} \qquad (3)$$

Here n is the total charge density, *e* the electron charge, *m* the mass of the electron and ε_0 the permittivity of vacuum.

Computational details

Calculations were performed based on the pseudo-potential plane-wave method within the framework of the density functional theory (DFT), as implemented in CASTEP code [21]. Normconserving pseudopotentials were employed to describe the electron–ion interactions. The exchange and correlation terms were described with the generalized gradient approximation (GGA). An energy cutoff E_{cut} = 550eV was chosen, and self-consistency was considered to be achieved when the total energy variation from iteration to iteration did not exceed $5x10^{-7}$ e/V/atom. For the substituted spinels $LiMn_{1.6}Ti_{0.4}O_4$ and $LiMn_{1.5}Ni_{0.5}O_4$, we constructed 5x1x1 and 2x1x1 supercells, respectively.

The crystal structures of the lithium manganate spinel and substituted spinels were taken from experimental results [22–24]. All three compounds present a cubic spinel-type structure and belong to the space group Fd-3m. Lattice parameters and atomic positions used in the calculations are summarized in Table 1.

Table 1
Lattice parameters and atomic coordinates for $LiMn_2O_4$, $LiMn_{1.6}Ti_{0.4}O_4$ and $LiMn_{1.5}Ni_{0.5}O_4$.

Compound	Lattice parameter (Å)	Atomic positions
$LiMn_2O_4$ [22]	8.2455	Li: 0.125, 0.125, 0.125 Mn: 0.5, 0.5, 0.5 O: 0.2634, 0.2634, 0.2634
$LiMn_{1.6}Ti_{0.4}O_4$ [23]	8.286	Li: 0, 0, 0 Mn: 0.625, 0.625, 0.625 Ti: 0.625, 0.625, 0.625 O: 0.389, 0.389, 0.389
$LiMn_{1.5}Ni_{0.5}O_4$ [24]	8.1659	Li: 0.125, 0.125, 0.125 Mn: 0.5, 0.5, 0.5 Ni: 0.5, 0.5, 0.5 O: 0.2632, 0.2632, 0.2632

Experimental

Spinel and doped spinel ($LiMn_2O_4$, $LiMn_{2-x}M_xO_4$, M = Ni or Ti) powders have been synthesized by sol–gel method using citric acid as chelating agent. Stoichiometric amounts of lithium acetate, manganese acetate, nickel acetate, and citric acid were mixed thoroughly and dissolved in de-ionized water. For the synthesis of Ti-doped spinel, the titanium butoxide and the other precursors were dissolved in isopropyl alcohol instead of water, in order to obtain the total dissolution of chemical reactives.

The starting solution was stirred continuously under heating at 60 °C to preserve a good homogeneity in the solution, and pH was regulated to 5 with a 25% NH_4OH solution. For the synthesis of gel, 14 ml of 1M citric acid were added to the homogenous solution drop by drop. The synthesized samples were dried overnight in an oven at 85 °C to remove the moisture and to obtain a dried mass. The dried mass was ground and treated at 950 °C for 10 h with a heating rate of 1 °C min.

Thin specimens suitable for electron microscopy were prepared by placing clean, dry, crushed powders onto commercial holey carbon-coated copper grids. Electron energy-loss spectra were obtained using a Gatan parallel electron energy-loss spectrometer (PEELS model 766) attached to a Philips CM-200 transmission electron microscope. Spectra were acquired in diffraction mode with 0.2 eV/ch dispersion, an aperture of 2mm, and a collection semi-angle of about 2.7 mrad. The resolution of the spectra was determined by measuring the full-width at halfmaximum (FWHM) of the zero loss peak, which was typically close to 1.2 eV, when the TEM was operated at 200 kV. EELS spectra were corrected for dark current and readout noise. The channel to

channel gain variation was minimized by normalizing the experimental spectrum with the independently obtained gain spectrum of the spectrometer.

Results and discussion

Samples were analyzed by X-ray diffractometry (XRD) to verify that we obtained the right spinel-type structure, and as can be seen in Fig. 1, a small shift of some prominent peaks in substituted spinels, with respect to $LiMn_2O_4$ is observed. Also, in Nisubstituted spinel, a small signal coming from a secondary phase is observed, which we have identified as NiO. Kim and Lee [14] suggested that this can be a phase transition to a tetragonal structure; however, according to our analysis, we were not able to distinguish deviations from the value c/a = 1.

Spectra acquired with the EELS spectrometer were Fourier-log deconvoluted to have the single scattering distributions S(E) and the energy-loss function Im(-1/ε). The real and imaginary parts of the dielectric function were obtained, after removing surface-loss effects, by Kramers–Kronig Analysis, as described by Egerton [15].

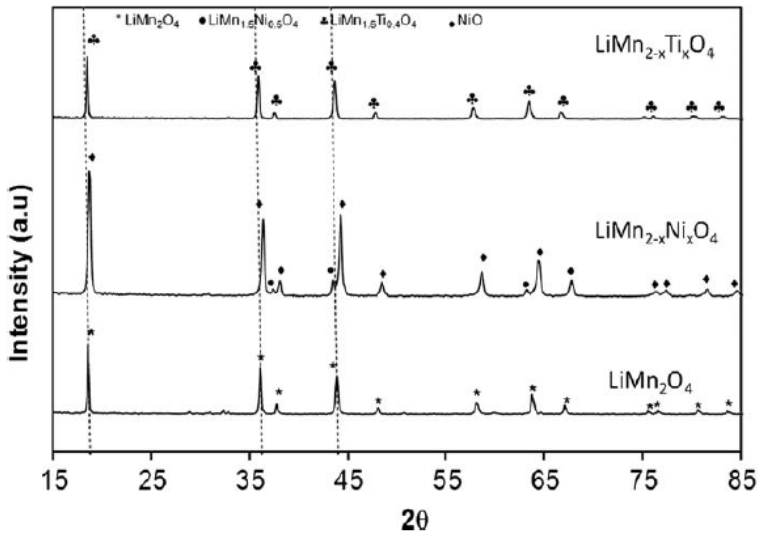

Fig. 1. XRD spectra of $LiMn_2O_4$, $LiMn_{1.6}Ti_{0.4}O_4$ and $LiMn_{1.5}Ni_{0.5}O_4$.

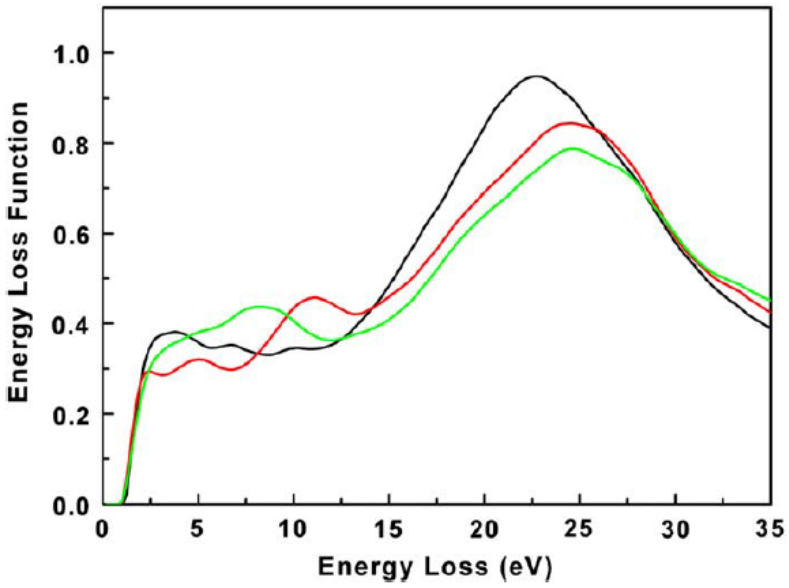

Fig. 2. Energy-loss function $\mathrm{Im}(-1/\varepsilon)$, for $LiMn_2O_4$ (black), $LiMn_{1.6}Ti_{0.4}O_4$ (red) and $LiMn_{1.5}Ni_{0.5}O_4$ (green). (For interpretation of the references to colour in this figure legend, the reader is referred to the web version of this article.)

The energy-loss functions for $LiMn_2O_4$, $LiMn_{1.6}Ti_{0.4}O_4$ and $LiMn_{1.5}Ni_{0.5}O_4$ are shown in Fig. 2. The dominant feature in all energy-loss spectra is the volume plasmon at 22.8, 24.4 and 24.6 eV for $LiMn_2O_4$, $LiMn_{1.6}Ti_{0.4}O_4$ and $LiMn_{1.5}Ni_{0.5}O_4$, respectively, complicated by interband transitions, as expected for transition metals. Features in the low-energy region arise from interband transitions and are characteristic of the energy-band structure of the materials.

As is well known, the plasmon peak position is shifted upward due to excitations below the plasma frequency and downward due to higher energy excitations, so the energy-loss spectrum cannot be directly associated with interband transitions. However, as the imaginary part of the dielectric function can be directly associated with interband transitions we should be able to relate these transitions with peaks in the ε_2 spectra. Fig.

3 shows the imaginary part of the dielectric function for the three compounds under study.

Even though it is possible to distinguish some structure directly from the ε_2 vs. E curves, it is still possible to enhance these peaks by plotting the optical joint density of states (J_1), defined in Eq. (2).

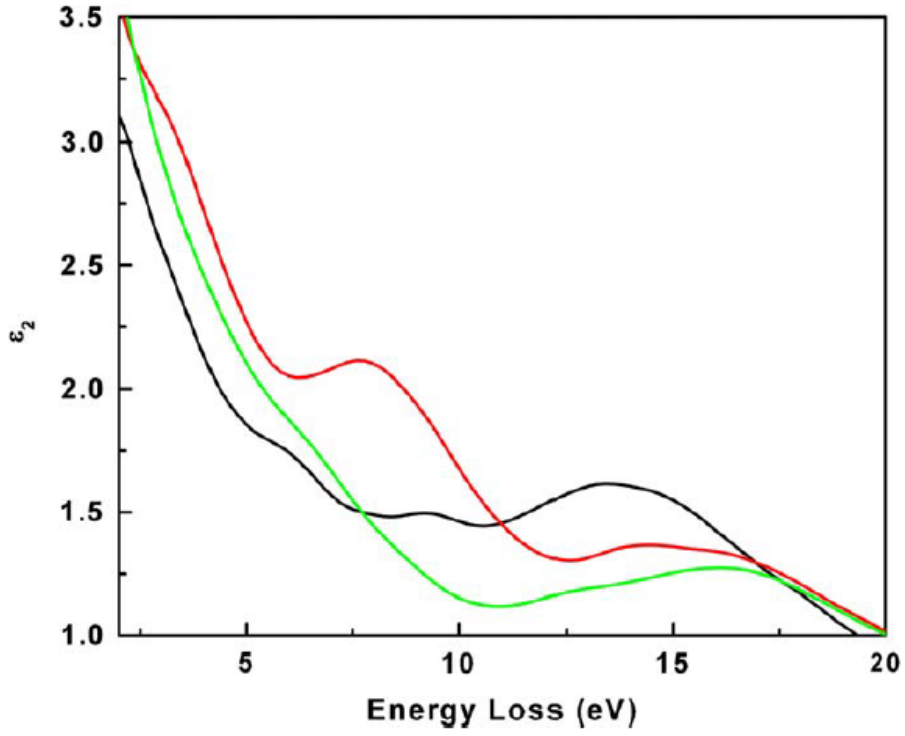

Fig. 3. Imaginary part of the dielectric function ε_2, for $LiMn_2O_4$ (black), $LiMn_{1.6}Ti_{0.4}O_4$ (red) and $LiMn_{1.5}Ni_{0.5}O_4$ (green). (For interpretation of the references to colour in this figure legend, the reader is referred to the web version of this article.)

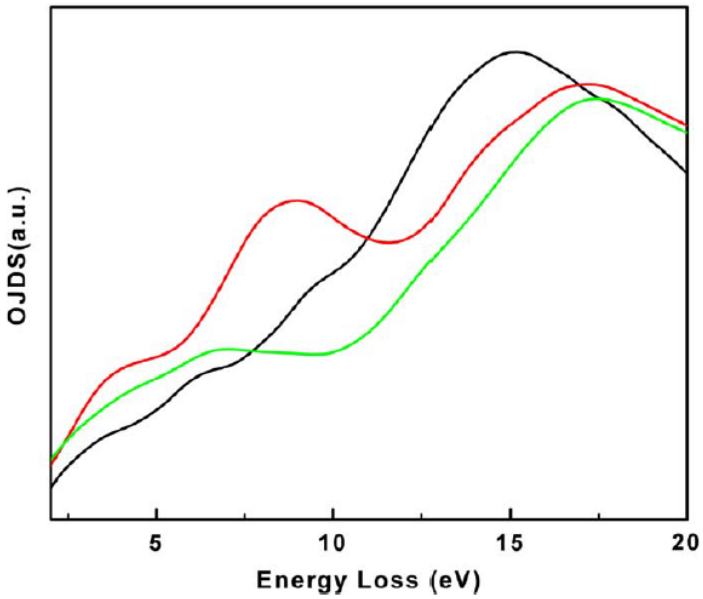

Fig. 4. Optical joint density of states $J_1(E)$, for $LiMn_2O_4$ (black), $LiMn_{1.6}Ti_{0.4}O_4$ (red) and $LiMn_{1.5}Ni_{0.5}O_4$ (green). (For interpretation of the references to colour in this figure legend, the reader is referred to the web version of this article.)

Fig. 4 shows $J_1(E)$ for the three compounds. It is noted that some peaks associated with interband transitions have been enhanced. Taking the second derivative of $J_1(E)$ with respect to E, peaks not visible in the $J_1(E)$ vs. E plots show relative maxima in $-d^2J_1(E)/dE^2$ vs. E plots. A close inspection of these curves, shown in Fig. 5, allows the identification of more structure. For $LiMn_2O_4$, peaks at 3.4, 4.6, 6.0, 7.8, 9.4, 13.2 and 14.8 eV are clearly visible; for $LiMn_{1.6}Ti_{0.4}O_4$ maxima can be identified at energies 3.4, 8.0, 9.2, and 13.8 eV and for $LiMn_{1.5}Ni_{0.5}O_4$ we can distinguish well-defined maxima at 4.0, 6.6, 8.8, 10.6 and 12.6 eV. Of course, wiggles in the second derivative of the OJDS have no physical meaning but are just a mathematical procedure to enhance the structure not visible, at first sight, in the OJDS vs. E plot. However, peak positions in the derivative correspond with peak positions in OJDS. Now, assuming the oscillator strength for a transition from an occupied state in a band to an unoccupied

state in another band is frequency-independent then the OJDS is proportional to the joint density of states (JDOS).

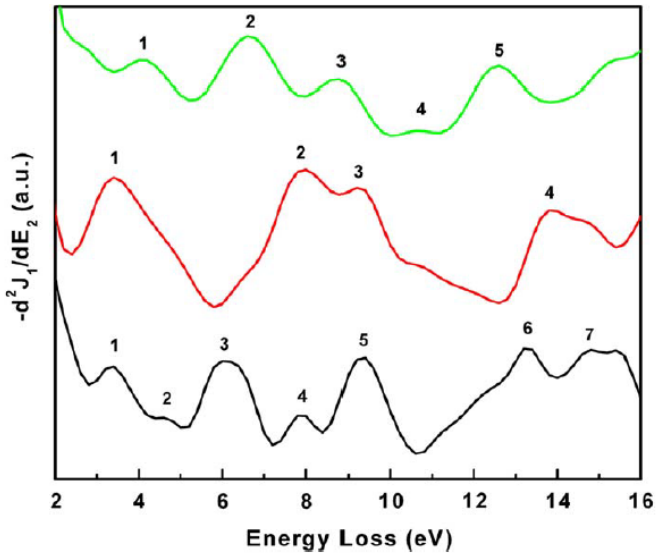

Fig. 5. Second derivative of the optical joint density of states for $LiMn_2O_4$ (black), $LiMn_{1.6}Ti_{0.4}O_4$ (red) and $LiMn_{1.5}Ni_{0.5}O_4$ (green). (For interpretation of the references to colour in this figure legend, the reader is referred to the web version of this article.)

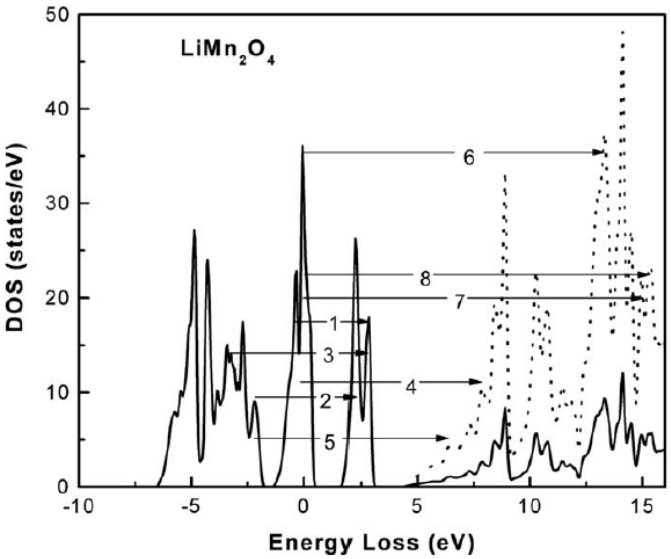

Fig. 6. Total DOS for $LiMn_2O_4$. The interband transitions for the peaks in Fig. 5 are indicated.

The electronic structure information available in the low-loss EELS spectrum is related to the joint density of states, which is high for energies at which two energy

surfaces lie parallel to each another at a particular k point in reciprocal space. At such points one has the so-called critical points. Since single electron interband transitions depend on critical points in the band structure, peaks in the imaginary part of the dielectric function give rise to the presence of critical points in the band structure. As peak positions in $LiMn_2O_4$, $LiMn_{1.6}Ti_{0.4}O_4$ and $LiMn_{1.5}Ni_{0.5}O_4$ are all different, as seen in the second derivative curves, energy-band structure, and therefore the density of states, changes when $LiMn_2O_4$ is doped with (Ti, Ni).

As maxima observed in the $J_1(E)$ vs. E plots are assigned to interband transitions above the Fermi level, these peaks can be interpreted on the basis of energy-band calculations.

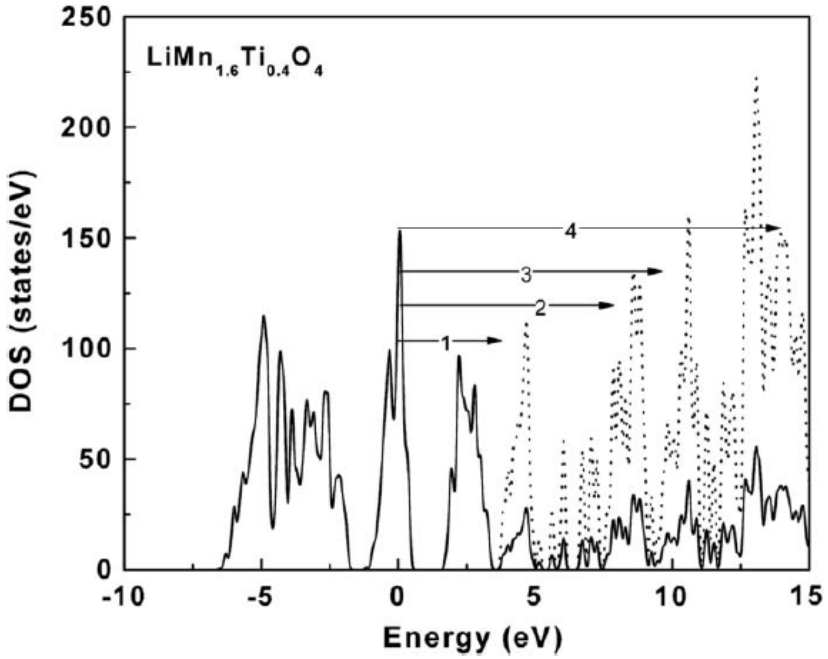

Fig. 7. Total DOS for $LiMn_{1.6}Ti_{0.4}O_4$. The interband transitions for the peaks in Fig. 5 are indicated.

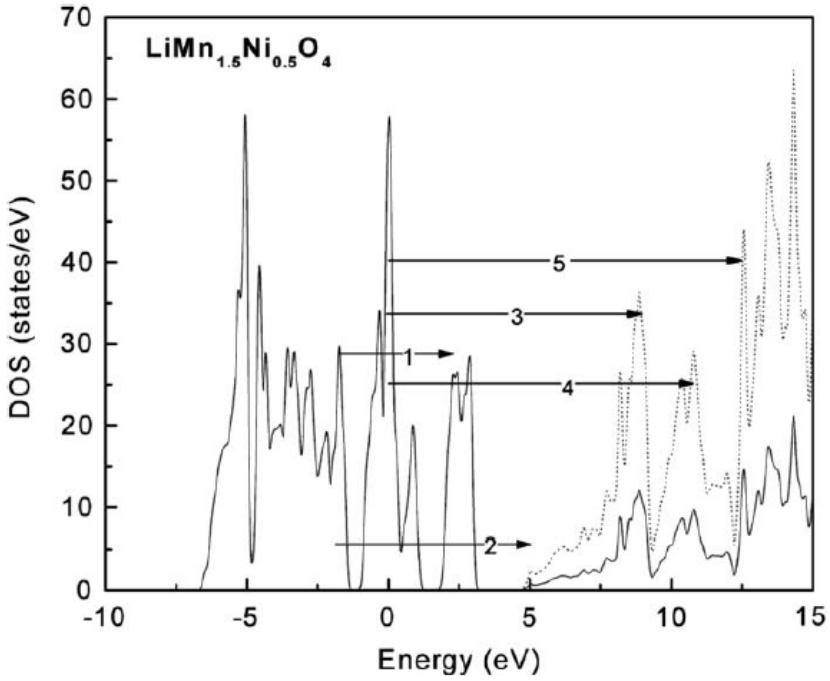

Fig. 8. Total DOS for $LiMn_{1.5}Ni_{0.5}O_4$. The interband transitions for the peaks in Fig. 5 are indicated.

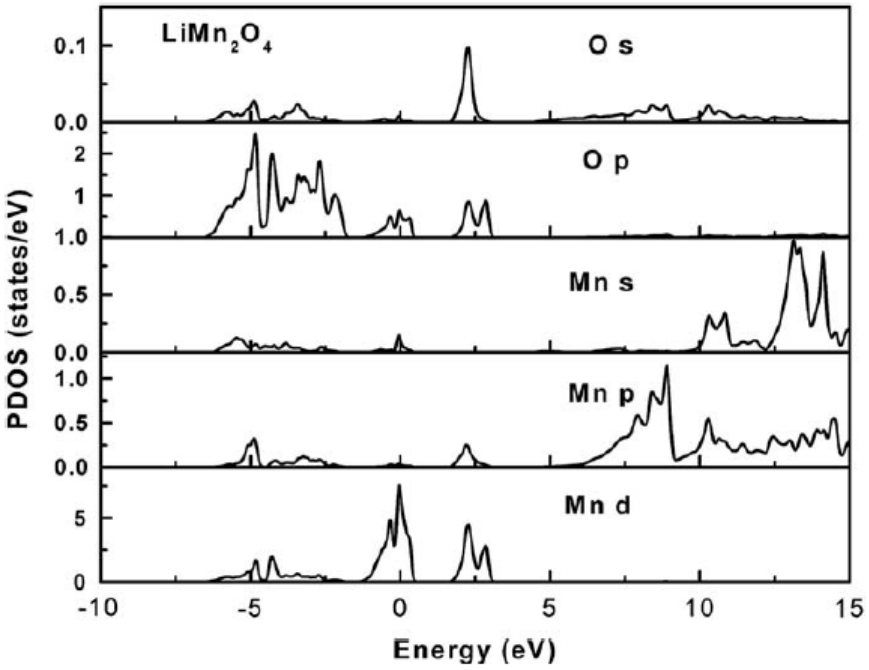

Fig. 9. Calculated partial density of states for $LiMn_2O_4$.

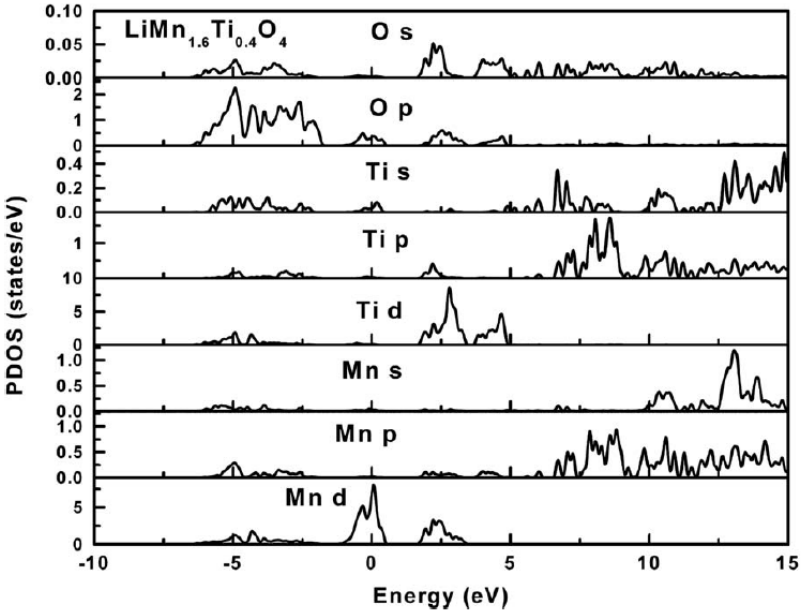

Fig. 10. Calculated partial density of states for $LiMn_{1.6}Ti_{0.4}O_4$.

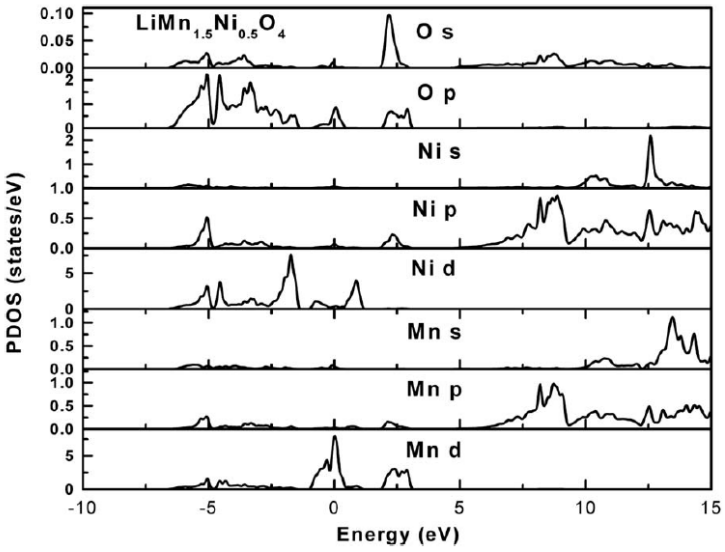

Fig. 11. Calculated partial density of states for $LiMn_{1.5}Ni_{0.5}O_4$.

In order to track differences in the electronic structure of the compounds, observed in the second derivative of the OJDS, we calculated the total and partial densities of states (PDOS). Figs. 6–8 show the total DOS for $LiMn_2O_4$, $LiMn_{1.6}Ti_{0.4}O_4$ and $LiMn_{1.5}Ni_{0.5}O_4$, respectively, where we show an assignment of the maxima identified

in the second derivative of the optical joint density of states, in terms of the interband transitions above the Fermi energy. Figs. 9–11 show the calculated PDOS. Even though the shape and intensities of the partial densities of states in lithium manganate change when doped with (Ti, Ni), the distribution in Ni-substituted spinel is similar to the lithium manganate, except for 3d states around 2.5 eV, missing in Ni. On the other hand, for Ti-substituted spinel, 3d states around 4–5 eV appear, which do not exist in lithium manganate nor in Ni-substituted spinel. There are, therefore, more dramatic changes in the electronic structure in lithium manganate spinel when doped with Ti. From Figs. 6–11, maxima identified in OJDS originate mainly from transitions between Mn 3d to Mn 4p and O 2p to Mn 4s orbitals in $LiMn_2O_4$; between Mn 3d to (Mn 4p, Ti 4s), O 2p to (Ti 4s, Ti 3d, Mn 4s) orbitals in Ti-substituted spinel and between Mn 3d to (Mn 4p, Ni 4p), Ni 3d to (Mn 4p, Ni 4p) and O 2p to (Ni 4s, Mn 4s) orbitals in Ni-substituted spinel.

The understanding of changes in electronic structure of lithium manganese oxide when doped with other elements can be used to clarify the behavior of these compounds for its application as cathode material in Li-ion batteries.

Conclusions

The electronic structure of sol–gel synthesized $LiMn_2O_4$, $LiMn_{1.6}Ti_{0.4}O_4$ and $LiMn_{1.5}Ni_{0.5}O_4$ was studied by low-loss transmission electron energy-loss spectroscopy and ab initio calculations. We obtained Kramers–Kronig derived complex dielectric function and optical joint density of states for the three compounds. Peaks in the OJDS were enhanced by taking the second derivative with respect to energy loss and compared with the density of states obtained from the calculations. Good agreement

was found between our experimental results and those based on theoretical calculations, in CASTEP code.

Acknowledgements

The authors acknowledge the financial support by CONACYT and Gobierno del Estado de Chihuahua, through the project CHIH- 2006-C02-58660.

References

[1] L. Yun-Sung, S. Yang-Kook, N. Kee-Suk, Solid State Ion. 109 (1998) 285.

[2] B.J. Hwang, R. Santhanam, D.G. Liu, J. Power Sources 101 (2001) 86.

[3] X. Wang, X. Chen, L. Gao, H. Zheng, J. Mingrong, T. Shen, Z. Zhang, J. Cryst. Growth 256 (2003) 123.

[4] L. Guohua, H. Ikuta, M. Wakihara, J. Electrochem. Soc. 143 (1996) 178.

[5] T.J. Boyle, D. Ingersoll, M.A. Rodrigues, C.J. Tafoya, D.H. Doughty, J. Electrochem. Soc. 146 (1999) 1683.

[6] P. Arora, B.N. Popov, R.E. White, J. Electrochem. Soc. 145 (1998) 807.

[7] Y. Gao, J.T. Dahn, J. Electrochem. Soc. 143 (1996) 1783.

[8] K. Amine, H. Tukamoto, H. Yasuda, Y. Fujita, J. Electrochem. Soc. (1996) 1607.

[9] Q. Zhong, A. Bonakdarpour, M. Zhang, Y. Gao, J.R. Dahn, J. Electrochem. Soc. 144 (1997) 205.

[10] N. Hayashi, H. Ikuta, M. Wakihara, J. Electrochem. Soc. 146 (1993) 2102.

[11] G.E. Grechnev, R. Ahuja, B. Johansson, O. Eriksson, Phys. Rev. B 65 (2002) 174.

[12] S. Suzuki, M. Tomita, S. Okada, H. Arai, J. Phys. Chem. Solids 12 (1996) 1851.

[13] Y. Shiraishi, I. Nakai, K. Kimoto, Y. Matsui, J. Power Sources 97–98 (2001) 461.

[14] K.J. Kim, J.H. Lee, Solid State Commun. 141 (2007) 99.

[15] R.F. Egerton, Electron Energy Loss Spectroscopy in the Electron Microscope, Plenum Press, New York, 1996.

[16] C.C. Ahn, Transmission Electron Energy Loss Spectrometry in Materials Science and the EELS Atlas, Wiley-VCH Verlag GmbH & Co. KGaA, Weinheim, Germany, 2004.

[17] G. Brockt, H. Lakner, Micron 31 (2000) 435.

[18] J. Pflu¨ ger, J. Fink, W. Weber, K.P. Bohnen, G. Crecelins, Phys. Rev. B 30 (1984) 1155.

[19] W.Y. Liang, A.R. Beal, J. Phys. C 9 (1976) 2823.

[20] F. Espinosa-Magan˜ a, A. Duarte-Moller, R. Martı´nez-Sa´ nchez, M. Miki-Yoshida, J. Electron. Spectrosc. Relat. Phenom. 125 (2002) 119.

[21] M.D. Segall, P.J.D. Lindan, M.J. Probert, C.J. Pickard, P.J. Hasnip, S.J. Clark, M.C. Payne, J. Phys.: Condens. Matter 14 (2002) 2717.

[22] J. Akimoto, Y. Takahashi, N. Kijima, Y. Gotoh, Solid State Ion. 172 (2004) 491.

[23] K.S. Yoo, N.W. Cho, Y.J. Oh, Solid State Ion. 172 (1998) 43.

[24] W. Branford, M.A. Green, D.H. Neumann, Chem. Mater. 14 (2002) 1649.